An Analysis of the Role of Side Assisting Gas during CO_2 Laser Welding †

ZHANG Linjie*, ZHANG Jianxun ** and MURAKAWA Hidekazu ***

Abstract

An experimental study of the role of side assisting gas during CO_2 laser welding has been carried out, and it is found that side gas velocity can significantly affect the laser induced plasma and the weld cross-sectional geometry. To confirm whether or not side gas flow affects the laser welding process mainly through influencing the refraction and absorption occurring within the plasma above the keyhole mouth, a three dimensional model based on the conservation laws of mass, momentum and energy has been used to predict the spatial distributions of plasma temperature under different side gas velocities. Furthermore, a ray-tracing method was employed to estimate the variation of the laser beam width due to refraction, as well as the energy loss due to inverse Bremsstrahlung absorption at different side gas velocities. The results indicate that variation of side gas velocity has little influence on the refraction and absorption occurring within the plasma above the keyhole mouth. The sensitivity of the laser welding process to side gas velocity may be due to some mechanism other than influencing the refraction and absorption of laser beam in plasma.

KEY WORDS: (CO_2 Laser Welding), (Plasma Plume), (Side Assisting Gas), (High Speed Imaging), (Numerical Model), (Ray Tracing Method).

1. Introduction

Laser welding has been widely employed in modern industries. In the actual CO_2 laser welding process, a side assisting gas flow is often introduced into the interaction zone. The sensitivity of laser welding process to side gas flow conditions has been reported by many researchers[1].

A. Matsunawa and S. Katayama found that one of the effective ways to suppress porosity formation was to use pure Nitrogen gas as the shielding gas in high power CO_2 laser welding[2]. K. Kamimuki *et al* investigated the effects of side gas flow on the prevention of the porosity in Nd:YAG laser welding[3]. Szymanski *et al* indicated that better plasma cooling was obtained when helium was the shielding gas due to its smaller molecular mass than that of argon as well as its higher heat conductivity[4]. Hamadou *et al* experimentally studied the influences of side nozzle geometrical parameters and side gas velocity on the plasma size and weld seam characteristics[5]. Beck *et al* reported that optimized shielding gas flow conditions could be achieved by applying a shielding gas mixture of He and Ar in the ratio 3:1[6].

Improvement comes only after better understanding of the laser welding process itself. So it is worthwhile to explore associated mechanisms of the laser welding process. This paper is an effort to get a better understanding of the mechanism through which laser welding process is significantly affected by side gas flow. In this research, the behaviour of laser induced plasmas under different side gas velocity have been recorded with the aid of a high speed CCD camera. A ray-tracing method and a three dimensional model are used to analyze the role of side assisting gas during laser welding. The results indicate that variation of side gas velocity has little influence on the refraction and absorption occurring in the laser induced plasma above the keyhole mouth.

2. Experimental

Experiments have been carried out to analyse the

† Received on June 16, 2006
* Graduate Student, Xi'an Jiaotong University
** Professor, Xi'an Jiaotong University
*** Professor

Transactions of JWRI is published by Joining and Welding Research Institute, Osaka University, Ibaraki, Osaka 567-0047, Japan

effect of side assisting gas velocity on laser induced plasma. A schematic drawing of the experimental setup is shown in **Fig.1.** During laser welding process, a high speed CCD camera was used to take images of the laser induced plasma above the workpiece top surface up to 1000 frames per second. The camera was stationary relative to the laser beam. In **Fig.1,** "*h*" corresponds to the distance between the lower edge of the side nozzle and the workpiece top surface, "α" defines the side nozzle inclination angle with regard to the horizontal line, and "*H*" is the distance between the lower edge of the coaxial nozzle and the plate top surface. The travelling speed of the workpiece "V_S" is 1m/min. The inner diameters of the coaxial nozzle and the side nozzle are 4mm and 2.5mm respectively.

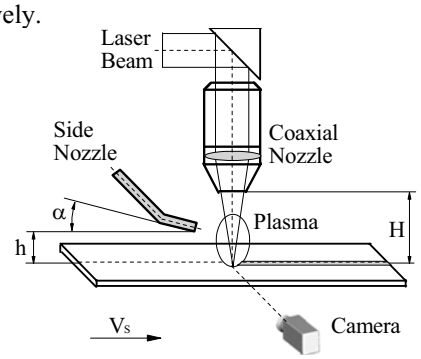

Fig.1 Schematic diagram of the experiment set-up.

Welding was done with a continuous wave CO_2 laser which delivers 3KW maximum mean power. The material used in this study was SUS304 stainless steel the dominant element of which was iron. The geometry of the welded plate was 200mm×100mm×2mm. Samples were manually cleaned with acetone before welding. Argon was used as shielding gas. Welding of bead-on-plate was performed.

Transient variations of optical emission intensity at different side gas discharge *V* are shown in **Fig.2** (a) and (b), while average optical emission intensity at different side gas discharge is plotted in **Fig.2** (c). The effect of side gas discharge on the weld geometry is shown in **Fig.3**. From **Fig.2,** it is clearly seen that the average optical emission intensity decreases with increasing side gas discharge. In addition, side gas discharge affects the weld geometry significantly. As shown in **Fig.3**, the weld cross section changes from "nail-head" shape to "echelon" shape when the side gas discharge increases from 5L/min to 10L/min.

3. Numerical Modelling

3.1 Assumptions

The assumptions employed in the numerical study include: (a) the keyhole welding process and the induced plasma are steady; (b) the flow is turbulent; (c) the plasma plume is in local thermodynamic equilibrium state; (d) metallic vapour and assisting gas is incompressible; (e) the keyhole is a fixed cylindrical blind hole and the laser beam is stationary relative to the keyhole; (f) the shielding gas is pure argon; (g) all of the metallic vapour is generated at the bottom of the blind keyhole, and lateral vapour ejection from keyhole walls is not considered; (h) the plasma in the keyhole absorbs a fraction of the laser energy through the Inverse Bremsstrahlung effect.

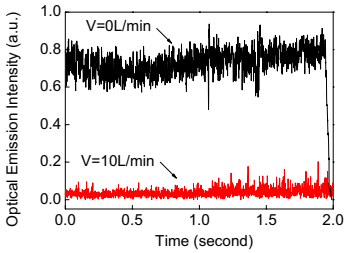

(a) Transient variations at *V*=0L/min and 10L/min

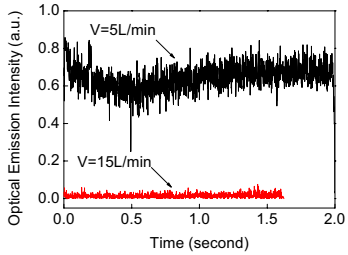

(b) Transient variations at *V*=5L/min and 15L/min

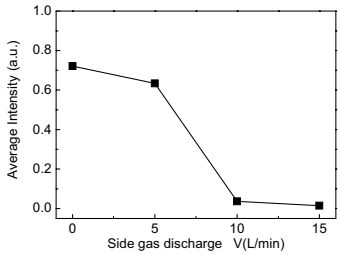

(c)Average intensity at different "*V*"

Fig.2 Effect of side gas discharge on optical emission intensity during laser welding.

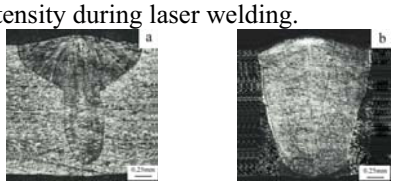

(a) *V*=5L/min (b) *V*=10L/min

Fig.3 Effect of side gas discharge on weld geometry.

3.2 Governing equations

Numerical simulations have been performed of a gas jet exiting from a side nozzle and blowing laser induced plasma above keyhole mouth. The model was solved by a finite volume method with an implicit scheme. The commercial software FLUENT was used for this purpose. Fundamental equations used by FLUENT are expressed below.

Continuity equation:

$$\frac{\partial \rho}{\partial t} + \nabla \cdot (\rho \vec{v}) = S_m \qquad (1)$$

where $\vec{v}$ is the velocity vector of gas, ρ is the gas density, S_m is the user defined mass source term to model the metal evaporation occurred at the bottom of keyhole.

Momentum equation:

$$\frac{\partial}{\partial t}(\rho\vec{v})+\nabla\cdot(\rho\vec{v}\vec{v})=-\nabla p+\nabla\cdot\left(\overline{\overline{\tau}}\right)+\rho\vec{g}+\vec{F} \quad (2)$$

where p is the static pressure, and $\rho\vec{g}$ and $\vec{F}$ are the gravitational body force and external body forces, respectively. The stress tensor $\overline{\overline{\tau}}$ is given by

$$\overline{\overline{\tau}}=\mu\left[\left(\nabla\vec{v}+\nabla\vec{v}^{T}\right)-\frac{2}{3}\nabla\cdot\vec{v}I\right] \quad (3)$$

where μ is the dynamic viscosity, I is the unit tensor.
Energy equation:

$$\frac{\partial}{\partial t}(\rho E)+\nabla\cdot(\vec{v}(\rho E+p))=$$

$$\nabla\cdot\left(k\nabla T+\sum_{j}h_j\vec{J}_j+\left(\overline{\overline{\tau}}\cdot\vec{v}\right)\right)+S_h \quad (4)$$

where the first three terms on the right-hand side represent energy transfer due to conduction, diffusion, and viscous dissipation, respectively. T is the gas temperature, k is the effective conductivity, $\vec{J}_j$ is the diffusion flux of species j, S_h is the user defined volumetric heat sources, and E is given by

$$E=h-\frac{p}{\rho}+\frac{v^2}{2} \quad (5)$$

where enthalpy h is defined as $h=\sum_j Y_j h_j$, Y_j is the mass fraction of species j.
Diffusion equation for metallic vapour:

$$\frac{\partial}{\partial t}(\rho Y_i)+\nabla\cdot(\rho\vec{v}Y_i)=-\nabla\cdot\vec{J}_i+S_m \quad (6)$$

where $\vec{J}_i$ is the diffusion flux of metallic vapour and Y_i is the mass fraction of metallic vapour. In turbulent flows, FLUENT computes the mass diffusion in the following form:

$$\vec{J}_i=-\left(\rho D_{i,m}+\frac{\mu_t}{Sc_t}\right)\nabla Yi \quad (7)$$

where Sc_t is the turbulent Schmidt number, μ_t is the turbulent viscosity and $D_{i,m}$ is the diffusion coefficient for metallic vapour in the mixture.

3.3 Boundary conditions

Presented in **Fig.4** is the mesh used for laser induced plasma simulation. The intersection of the laser beam axis and workpiece top surface is the origin of the Cartesian coordinate system. **Fig.5** shows the boundary conditions used in this study. The keyhole diameter is assumed to be 0.5mm.

Boundary conditions employed in the modeling are as follows. Metal vapour with fixed temperature enters into the computational domain at constant mass generation rate at the bottom of the keyhole. The mass generation rate at the bottom of the keyhole is determined by conservation of energy[1]. Using the user-defined function (UDF) provided by FLUENT, a mass source term S_m (kg/m^{3}s) is added at the lower part of the keyhole (i.e. rectangular region $C'CDD'$ shown in **Fig.5**) to simulate the metal evaporation occurred at the bottom of keyhole.

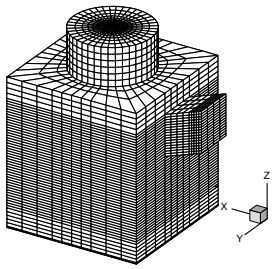

Fig.4 Three dimensional mesh used in plasma simulation (154488 cells).

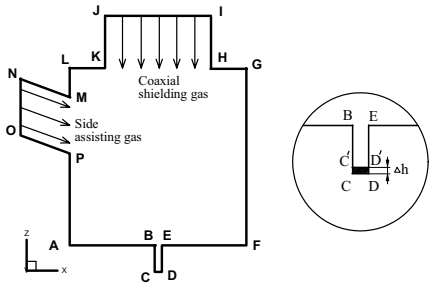

Fig.5 Schematics of the boundary conditions used for the laser-induced plasma simulation.

The boundary conditions at the blind keyhole wall (i.e. BC, CD and DE in **Fig.5**) are $v_x=0$, $v_y=0$, $v_z=0$ and $T=T_{va}$, where T_{va} is vaporization temperature. For the other part of the workpiece top surface (i.e. AB and EF in **Fig.5**), $v_x=0$, $v_y=0$, $v_z=0$ and $T=T_0$ are used as the boundary conditions, where T_0 is environment temperature. Along the outer wall of coaxial nozzle (i.e. HI and JK in **Fig.5**), $v_x=0$, $v_y=0$, $v_z=0$ and $T=T_0$ are used. And the same boundary conditions are used at the outer wall of the side nozzle (i.e. MN and OP in **Fig.5**). In order to protect the laser head from thermal damage by the high temperature plasma, shielding gas is introduced into the interaction zone by a nozzle coaxially placed with the laser beam. For the region IJ on the top boundary where the coaxial shielding gas enters into the computational domain, the boundary conditions $v_x=0$, $v_y=0$, $v_z=-V_c$ and $T=T_0$ are used, where V_c is the mass flow rate of the coaxial shielding gas. The laterally assisting gas is assumed to inject from the region NO in **Fig.5** with a fixed velocity V_g at an inclination angle of α, and thus $v_x=cos\alpha\cdot V_g$, $v_z=-sin\alpha\cdot V_g$ and $T=T_0$ are employed. For the other boundaries (i.e. FGH, KLM and PA in **Fig.5**), the boundary conditions $P_{gauge}=1.01\times10^5 Pa$ and $T_{bf}=T_0$ are used, where P_{gauge} is the gauge pressure and T_{bf} is the backflow temperature.

The vaporized metal would move through the incident laser beam before leaving the focal area. While the vaporized metal is in the laser beam, it may be heated to temperatures greatly in excess of the vaporization temperature, which produces a rapid increase in the level of ionization within the metal vapour. At high electron densities, an inverse Bremstrahlung process occurs and

removes energy from the incident laser beam and redirects this energy into heating of the gas. In equation (4), the source term S_h represents the absorption of incident laser radiation by the metal vapour in the keyhole through inverse Bremsstrahlung mechanism. The energy source term S_h is

$$S_h = \theta \cdot I \tag{8}$$

where

$$\theta = \left(3.3 \times 10^{-39}\, n_e^2\right) \Big/ T_e^{3/2} \tag{9}$$

here θ is inverse Bremsstrahlung absorption coefficient, I is laser intensity, n_e is electron density and T_e is electron temperature[1]. Using user defined function UDF, energy source term is added to the governing equation.

3.4 Results and discussion

3.4.1 Effect of side gas flow rate

In the computation, the side assisting gas velocity V_g is treated as a parameter and taken to be 0ms^{-1}, 10ms^{-1}, 20ms^{-1} and 40ms^{-1}, respectively. The velocity of coaxial shielding gas is assumed to be 5ms^{-1}. The side nozzle height is taken to be 5.5 mm, whereas the side nozzle angle is taken to be 20º.

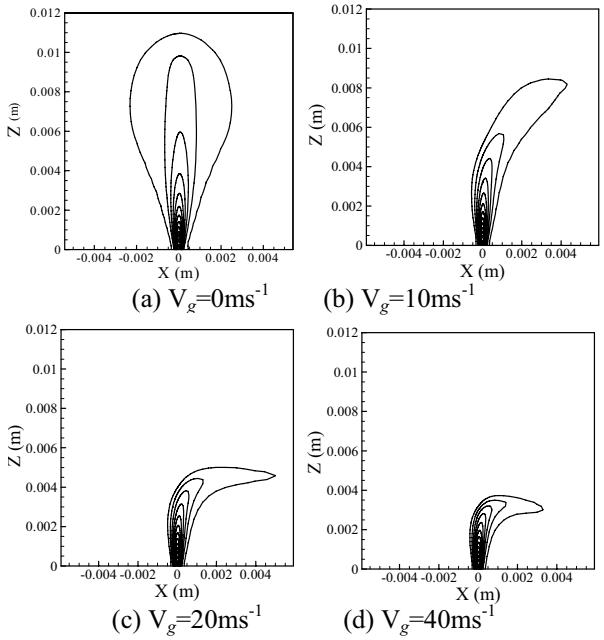

(a) V_g=0ms^{-1} (b) V_g=10ms^{-1}

(c) V_g=20ms^{-1} (d) V_g=40ms^{-1}

Fig.6 Computed isotherms on the middle vertical section (i.e. at the *x-z* plane with y=0mm) for different side gas velocities at the keyhole bottom. Outer isotherm is 1000K, and isotherm interval 1000K.

Fig.6 (a)-(d) show the computed isotherms on the middle vertical section (i.e. at the *x-z* plane with y=0mm) for the four different side gas velocities. From the computed results shown in **Fig.6** (a)-(d), it is seen that the velocity of side assisting gas can significantly affect the temperature fields as well as the sizes of .plasma plume. The plasma plume is blown away from its original location along the geometrical axis by the side assisting gas. With an increase in the side assisting gas velocity, the size of the plasma decreases. In addition, it is found that the maximum temperature of the plasma plume is influenced by side assisting gas only to a small extent. The maximum temperature of the plasma plume decreases from 13689K for the case without side assisting gas to 13659K for the case with V_g=40ms^{-1}.

Comparison of the computed result without including side assisting gas (i.e. **Fig.6** (a)) to those including side assisting gas (i.e. **Fig.6** (b)-(d)) reveals that due to the cooling effect of side assisting gas, the dimension of the plasma plume becomes smaller, consistent with the experiment results.

3.4.2 Laser absorption and laser refraction

Based on the distributions of plasma temperature at the middle vertical section, the electron number density at the section can be computed. Furthermore, we can evaluate the distributions of the absorption coefficient and the refraction index at this section. Finally, a ray-tracing computer program was written to compute laser beam refraction and energy absorption in the plasma until the laser beam reaches the workpiece top surface.

For weakly ionized plasma, the refractive index n_{ref} is approximately given by[1]

$$n_{ref} = \left(1 - n_e / n_c\right)^{1/2} \tag{10}$$

here n_c is a critical electron density：

$$n_c = m_e \varepsilon_0 \omega^2 / e^2 = 3.14 \times 10^{-10}\, \omega^2 \left(cm^{-3}\right) \tag{11}$$

where ε_0 is the permittivity of free space, and ω is frequency of the laser. For CO_2 laser radiation, $\omega = 1.78 \times 10^{14}\, rad \cdot \sec^{-1}$.

With the temperature dependent refractive index, the refraction of the laser beam in the plasma was computed by the ray tracing method. The laser beam shape is subdivided into a given number of sub-beams delimited by the rays constituting a pipe that contains a fraction of the beam energy, and the rays constituting the laser beam are followed from their entrance inside the plasma until they reach the workpiece surface after undergoing a great number of refractions in the plasma. In this study, 600 sub-beams constitute the laser beam and each ray undergoes 6000 refractions before reaching the workpiece surface.

The local values of the absorption coefficient of the plasma plume are calculated using equation (9). With the computed spatial variations of the absorption coefficient within the plasma plume, we can further calculate the energy absorption of the laser beam when it passes through the plasma plume. After passing through a control volume, the laser energy will be partially absorbed and the absorbed energy can be calculated by[1]

$$I_{out} = I_{in} \cdot \exp\left(-\theta \Delta z\right) \tag{12}$$

here I_{in} and I_{out} are the laser intensities as the laser beam enters into and departs from the control volume, respectively, Δz is the size of the control volume in the z-direction. Using equation (12) and repeating the calculation for all the control volumes along the sub-beam path, the fraction of absorbed laser energy for each sub-beam is obtained.

As an example, the computed spatial variations of absorption coefficient and refractive index at the middle vertical section for the case when side gas velocity V_g is 0ms^{-1} gas are shown in **Fig.7** (a) and **Fig.7** (b), respectively.

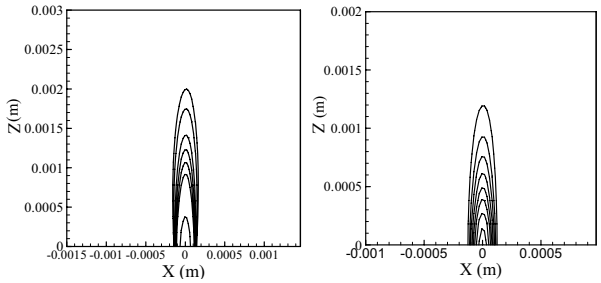

(a) Absorption coefficient (b) Refractive index

Fig.7 Computed distributions of the absorption coefficient and the refractive index at the middle vertical section (i.e. at the x-z plane with y=0m) (a) Absorption coefficient. Outer line is 20m^{-1}. Contour interval is 20m^{-1}; (b) Refractive index. Outer line is 0.999. Contour interval is -0.001. Side gas velocity V_g is 0ms^{-1}.

The original power density distribution of the laser beam is assumed to be Gaussian (TEM$_{00}$ mode) [7]. The initial diameter of the laser beam focal spot without refraction is assumed to be 0.3mm[8]. **Fig.8** shows the lateral displacement of rays constituting the laser beam when they reach the workpiece top surface. It can be seen from **Fig.8** that the diffraction occurring within the plasma at different side gas velocities are similar. **Fig.9** shows the laser beam width at the workpiece surface for different side gas velocities. **Fig.10** shows the power density at workpiece surface for different side gas velocities, while **Fig.11** shows the fraction of absorbed laser energy at different side gas velocities.

Results shown in **Fig.8-11** reveal that the effect of side gas velocity on the refraction and absorption occurring in plasma is small. When the side gas velocity increases from 0ms^{-1} to 40ms^{-1}, the laser beam width at middle vertical section decreases only from 3.16×10^{-4}m to 3.12×10^{-4}m and the fraction of absorbed laser energy decreases from 19.5% to 17.7%. This phenomenon can be explained as follows. The beam width and power density at the workpiece top surface mainly depend on the temperature distribution of the high temperature region within the plasma plume. As shown in **Fig.6**, the temperature distribution of the high temperature region within the plasma plume at different side gas velocities are similar, resulting in the small effect of side gas velocity on the laser beam width and power density at workpiece surface. Therefore, the effect of side gas velocity on the laser welding process shown in **Fig.2-3** can not be interpreted as diffraction and absorption being sensitive to side gas velocity.

Kamimukia *et al* experimentally verified that the melt pool flow behaviour with side gas flow was quite different from that without side gas flow[3]. When a proper side gas jet was used, the keyhole diameter was enlarged and stabilized by the side gas jet and thus the flow of the melt pool was smooth, continuous and without oscillations at the surface of the melt pool. Hence we think that the sensitivity of the laser welding process to side gas velocity may be mainly due to the side gas/molten pool interaction, and a detailed study of the interaction between side assisting gas and molten pool and its effects on the laser induced plasma, the weld geometry and the stability of the laser welding process will be our future work.

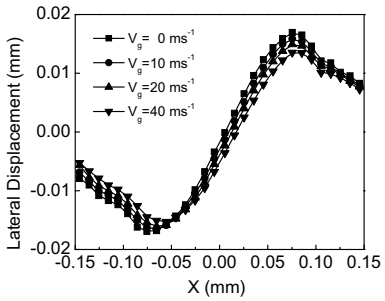

Fig.8 Lateral displacement at different "V_g".

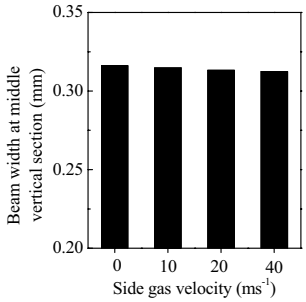

Fig.9 Beam width in middle vertical section at different "V_g".

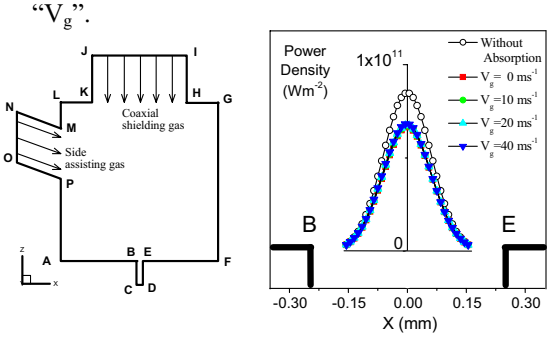

Fig.10 Power density after absorption in the plasma above workpiece surface for different "V_g".

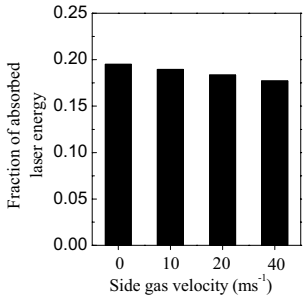

Fig.11 Fraction of absorbed laser energy at different "V_g".

4. Conclusions

A three dimensional model was developed to calculate the spatial distributions of plasma temperature under different side gas velocities. Modelling results concerning the influences of side gas velocity are reasonably consistent with experiment results. A ray-tracing method was used to evaluate the variation of the laser beam width due to refraction and the energy loss due to inverse Bremsstrahlung absorption at different side gas velocities. The results indicate that the refraction and absorption occurring within the plasma are influenced by side gas velocity only to a small extent.

Acknowledgments

The authors acknowledge the financial support of the National Natural Science Foundation of China under Grant No.50475093 and China Doctoral Education Base Foundation under Grant No.20030698018.

References

1) W. W. Duley, (1999): "*Laser welding,"* John Wiley & Sons, New York.
2) A. Matsunawa, S. Katayama, (2001): "Keyhole Instability and Its Relation to Porosity Formation in High Power Laser Welding," ASM Conference Proceedings: Joining of Advanced and Specialty Materials, pp. 8-15.
3) K. Kamimukia, T. Inoue and A. Matsunawa, (2002): "Prevention of welding defect by side gas flow and its monitoring method in continuous wave Nd: YAG laser welding," Journal of Laser applications, Vol. 14, pp. 136-145.
4) Z. Szymanski and J. Kurzyna, (1994): "Spectroscopic measurements of laser induced plasma during welding with CO_2 laser," Journal of Applied Physics, Vol. 76, pp. 7750-7756.
5) M. Hamadou, R. Fabbro and G. Caillibotte, (2002): "Study of Assisting gas Flow Behaviour during Laser Welding" Proceedings of ICALEO2002, Arizona, USA.
6) M. Beck, P. Berger and H. Hugel, (1995): "The effect of plasma formation on beam focusing in deep penetration welding with CO_2 lasers" Journal of Physics D: Applied Physics, Vol.28 pp. 2430-2442.
7) S. Kou, (2002): "*Welding metallurgy,"* John Wiley & Sons, New Jersey.
8) J. Kroos, U. Gratzke and G. Simon, (1993): "Towards a self-consistent model of the keyhole in penetration laser beam welding," Journal of Physics D: Applied Physics, Vol.26 pp. 474-480.